RSC Advances

PAPER

View Article Online
View Journal | View Issue

Cite this: *RSC Adv.*, 2025, **15**, 37412

Computational insights into the electrochemical performance of As_4O_6 as a novel anode material for Li-ion and Mg-ion batteries

Harram Najum,[a] Abdul Majid, *[a] Nimra Zaib Raza,[a] Muhammad Isa Khan,[b] Ahmed Ahmed Ibrahim[c] and Kamran Alam[d]

Received 28th August 2025
Accepted 21st September 2025

DOI: 10.1039/d5ra06452j

rsc.li/rsc-advances

The growing demand for high-performance next-generation batteries requires the development of advanced anode materials with improved capacities. In this study, the electrochemical performance of As_4O_6 inorganic molecular cages (IMCs) is investigated using first-principles strategies for their application as anode materials in lithium-ion batteries (LIBs) and magnesium-ion batteries (MIBs). The electronic structure, structural stability, charge-storage mechanism, electrochemical performance and redox behavior of As_4O_6 IMCs are thoroughly investigated. The proposed material As_4O_6 appeared thermodynamically stable and exhibited a strong affinity toward ion storage, highlighted by the exothermic interaction of Li and Mg metal ions within the As_4O_6 host. Molecular dynamics simulations further confirmed the remarkable thermal and structural stability of both the pristine and fully loaded host structures. The calculated storage capacity is computed as 457 mA h g^{-1} for the LIBs and 1012 mA h g^{-1} for the MIBs. The open circuit voltage (OCV) was found to be 0.66 V for the LIBs and 0.23 V for the MIBs, which further validates the potential of the material for use in batteries. The host offered a low energy barrier of 0.35 eV for Li diffusion and 0.13 eV for Mg diffusion, which indicates quicker ionic transport and diffusion coefficients of 1.09 × 10^{-7} m^2 s^{-1} for Li and 1.13 × 10^{-7} m^2 s^{-1} for Mg. The comprehensive findings highlight the suitability of As_4O_6 as a promising anode material for high-energy storage in monovalent and multivalent ion batteries.

1. Introduction

Molecular crystals comprising IMCs exhibit great potential due to their adjustable and specific properties for uses in modern applications.[1–3] The material properties are strongly influenced by their structures, and new features appear when their dimensions are reduced. They are composed of small repeating units, in the form of molecular clusters, that are considered zero-dimensional versions of their bulk structures.[1,4,5] Bottom-up techniques can be used to integrate such molecular units into 2D and 3D bulk structures. Strong bonds hold the atoms inside each molecule, while weak van der Waals (vdW) forces participate in inter-molecular bonding. These crystals offer several advantages including quantum confinement, surfaces without dangling bonds, quantum tunneling, and structure–properties relationships, along with other unique characteristics.[6,7] 2D molecular crystals have gained immense value in the field of microelectronics and nanotechnology but their thermal instability, one of their major limitations, hinders their performance.[8,9] IMCs belong to a unique class of materials owing to their unique 0D geometry. The cages are chemically inert and stable restricting bonding with other atoms. Their numerous advantages such as adjustable electronic characteristics, well-defined internal gaps, low density, high thermal and chemical stability and capacity to host guest atoms or ions make them promising candidates for a wide range of advanced technological applications.[10–12] In particular, arsenic trioxide (As_4O_6)-based IMCs have a unique polyhedral architecture with permeable hollow spaces. These internal voids allow ion diffusion and storage, which are two key requirements for obtaining effective electrode materials.[13]

Currently, the growing demand for sustainable energy solutions driven by global energy consumption and environmental challenges continue to push the humanity towards more sustainable and alternative energy-acquiring methods.[14–16] Wind turbines, coal and solar cells are the renewable energy sources that have a significant impact on global energy consumption. However, they inherently face challenges due to their variable nature.[17,18] The electrification of transportation

[a]*Department of Physics, University of Gujrat, Gujrat 50700, Pakistan. E-mail: abdulmajid40@yahoo.com*

[b]*Department of Physics, Islamia University of Bahawalpur, Rahim Yar Khan Campus, Bahawalpur, Pakistan*

[c]*Department of Physics and Astronomy, College of Science, King Saud University, P. O. Box 2455, 11451 Riyadh, Saudi Arabia*

[d]*VITO (Flemish Institute for Technological Research), Separation and Conversion Technology, Boeretang 200, 2400 Mol, Belgium*

and environmental concerns have positioned rechargeable batteries as a cornerstone technology.[19–23] Among various storage technologies, lithium-ion batteries (LIBs) have dominated the market due to their excellent charging–discharging performance, long cycle life, high energy density and outstanding electrochemical properties.[23,24] However, their inherent limitations, such as their reliance on costly and limited lithium resources, low theoretical capacity, safety concerns and associated performance constraints, highlight the need for the exploration of alternative energy solutions.[25–27] Multivalent ion batteries, such as zinc-ion batteries, magnesium-ion batteries (MIBs), and aluminum-ion batteries (AIBs), are emerging as alternative candidates. They play a pivotal role in this shift due to their ability to better accommodate the variable nature of renewable energy sources, including wind power, coal and solar energy.[28–30] Among them MIBs, due to the bivalency of Mg ions, stand out, offering higher volumetric capacity than LIBs along with better energy density compared to the widely used nickel–cadmium and lead–acid systems.[31] Magnesium is ranked eighth and is highly abundant in the Earth's crust; it is environmentally friendly and safe to handle.[32,33]

The performance of these batteries heavily depends on the electrode materials. The anode is one of the essential components of a battery that plays an important role in determining the overall electrochemical performance.[34] The development of lightweight, compact and long-cycle-life batteries has become urgent to meet the demands for sustainable energy solutions in advanced technology.[18,35] Advancing battery technology requires either the development of superior anode materials or the selection of metal ions with a higher charge than lithium.[28,36] Currently, the most widely used anode material is graphite which offers a modest capacity of about 372 mA h g^{-1}. However, its further advancement is hindered by its limitations such as sluggish ion diffusion.[37] Moreover, the intense coulombic interaction among the electrodes and Mg^{2+} ions poses additional challenges in the development of high-performance anode materials for MIBs, resulting in lower efficiency and sluggish ion transport.[38] Thus, exploring novel anode materials is essential to enhance the battery charge, storage ability and overall performance.[39,40] Recent studies have explored silicon-based materials, transition metal oxides (TMOs) and two-dimensional (2D) graphene-based anode materials. TiO_2 and MoS_2 are TMOs that exhibit a high theoretical capacity but volume expansion leads to poor cycling stability. Despite its tremendous capacity (4200 mA h g^{-1}), silicon experiences a severe volumetric expansion of about 300% which results in structural degradation and reduced lifetime.[41–44] Graphene and other 2D materials indeed offer high conductivity and a high surface area but restacking problems limit their active surface area, hindering their practical use in improving electrochemical performance.[45] Some reported anode materials are highlighted in Table 1.

To overcome such challenges, zero-dimensional materials such as quantum dots, metal organic frameworks and molecular cages, have gained interest as a prospective solution.[12] These materials are appealing for energy-storage applications owing to their unique electronic and structural properties including a high surface-to-volume charge ratio, improved ion diffusion and quantum confinement effects.[46] However, their practical application can be hindered by several constraints, including their low conductivity and structural instability.[47,48] Finding 0D materials with reliable and trustworthy electrochemical characteristics that work well for both MIBs and LIBs is a challenging task. Among various potential candidates, an intriguing family of materials, *i.e.*, zero-dimensional molecular cages, particularly arsenic trioxide As_4O_6, has emerged as a potential avenue for developing advanced anode materials because of their well-defined structural cavities and possibility for customized synthesis. Studies investigating alternatives to LIBs, such as MIBs, have been spurred due to their safety and resource availability issues. By leveraging its distinct structural properties, this research explores the electrochemical performance of As_4O_6-based IMCs with the goal of potentially overcoming the issues facing conventional anode materials.[49] The utilization of arsenic and arsenic-based materials as high-capacity anodes has been reported. Though elemental arsenic and As/C composites have been reported to exhibit a storage capacity of 1000 mA h g^{-1} for Li-ion batteries, they require conductive carbon matrices to improve cycling life and buffer large volume changes.[50] When combined with graphene or carbon nanotube, alpha-AsP (253 mA h g^{-1} for Mg) and black-arsenic composites show high capacities and stable performance due to nanosizing and matrix reinforcement. GO/B-AsP/CNTs exhibit a theoretical capacity of 1286 mA h g^{-1} with 80% retention but suffer from poor conductivity and volume changes.[51,52] In comparison, As_4O_6 demonstrates theoretical capacities of 457 mA h g^{-1} and 1012 mA h g^{-1} for LIBs and MIBs respectively with excellent cycling stability and rate performances. This investigation shows that battery performance can be enhanced by the exothermic interaction between the host material and intercalated ions.

This research explores the electrochemical behavior of As_4O_6 as a novel anode material for both LIBs and MIBs. While this is the first study to predict the fundamental electrochemical properties of As_4O_6, comprehensive strategies for its safe synthesis, handling and disposal need to be devised. It is well known that arsenic-based substances are generally toxic. However, material handling and engineering techniques can help reduce the expected risks when they are used in electrochemical devices.[60] Several approaches include surface passivation with inert films, encapsulation using conductive carbon matrices, and enhancement of the solid-state electrolyte. These techniques effectively suppress the dissolution and leaching of arsenic upon cycling. Similar strategies have been successfully extended to other high-efficiency but toxic semiconductor materials such as Pb-based halide perovskites in photovoltaics and Cd-based materials in optoelectronics, to ensure their practicality in all applications with no limitation of toxicity.[61–63] Thus, with rational engineering design of As_4O_6 clusters can be developed into a kind of safe and high-performance anode material for rechargeable batteries. Four arsenic atoms and six oxygen atoms combine to form a unique molecular cage-like structure with well-defined cavities that facilitate the diffusion

Table 1 Comparison of As_4O_6 IMCs with other reported anode materials

Material	Battery	Capacity (mA h g^{-1})	Adsorption energy (eV)	Energy barrier	OCV	Diffusion coefficient	Ref.
As_4O_6 IMCs	MIB	1017	−0.83	0.13	0.23	1.13×10^{-7}	This work
As_4O_6 IMCs	LIB	457.21	−0.42	0.35	0.66	1.09×10^{-7}	This work
P_4Se_3 IMCs	MIB	519	−0.65	0.30	0.27	5.27×10^{-9}	12
MoS_2	MIB	469	−1.430	0.039	—	—	53
o-Al_2N_2	MIB	715	—	0.17	0.37	—	54
Ge/C	LIB	770	—	—	—	—	55
Co_9S_8	LIB	303.5	—	—	—	—	56
Bi-nanotubes	LIB	303	—	—	—	—	57
Mg_3Bi_2	MIB	263	—	—	0–1.6	—	58
P-Bi_3Sn_2	MIB	301	—	—	0–0.8	—	59

and insertion of metal ions.[64] The 0D nature of As_4O_6, apart from its other potential benefits distinguishes it from other anode materials. While the theoretical capacity of As_4O_6 is not much higher than those of other materials in different dimensions its unique molecular structure makes it a strong candidate for additional investigation in monovalent and multivalent batteries. The electrode electrolyte kinetics of electrochemical reactions can be enhanced by the small size of As_4O_6, which results in a high surface area. Unlike other traditional anode materials, these cages offer an adjustable and highly ordered framework which can speed up ion extraction and insertion improving electrochemical characteristics.

First principles calculations are instrumental in predicting a material's electronic and electrochemical properties to explore its application potential for energy-storage devices.[65–67] In this study, a density functional theory (DFT)-based methodology is utilized to obtain a fundamental understanding of the structural, electronic, thermal and electrochemical properties of the As_4O_6 IMCs.[68] The most stable atomic structure and electronic properties of the material are obtained by geometry optimization.[37] The intercalation feasibility of Li and Mg atoms into the host structure is investigated to confirm the material's potential as a promising anode material. The diffusion behaviors of Li and Mg ions are studied using nudged elastic band (NEB) simulation.[66,67] The NEB simulation is also used to further understand the material's electronic conductivity, thermodynamics stability and ion mobility. The following sections discuss the results and computational details.

2. Computational details

This study is based on DFT calculations performed *via* Amsterdam Density Functional (ADF) modules for investigating the electrical, structural and conductive properties of As_4O_6 molecular cages as possible anode materials for metal-ion batteries.[69,70] Generalized Gradient Approximation under the Perdew–Burke–Ernzerhof (GGA-PBE) parametrization was employed with triple-zeta polarization (TZP) basis sets.[71,72] However, considering the renowned underestimation of band gaps associated with using PBE, we used hybrid functional B3LYP to ensure higher accuracy. This theoretical strategy was configured through the graphical user interface (GUI) of the ADF package. Geometry optimization was carried out *via* the quasi-Newton method, with a step size of 0.001 and a convergence criterion of 10^{-5} eV per atom for the total energy.[73] These simulations were performed to calculate the adsorption energy and the energy values before and after the intercalation of metal ions in the As_4O_6 host. The energy values were deduced *via* structural optimization. Single-point energy calculations were conducted to evaluate the total energies before and after the intercalation of the metal ions in the As_4O_6 host.[74,75] The lithiation and magnesiation energy, E(M), corresponding to the insertion of Li and Mg atoms (M) in favorable locations inside the As_4O_6 host, was determined by eqn (1).[76,77]

$$E(\mathrm{M}) = E_{n\mathrm{M}_{\mathrm{As_4O_6}}} - n \times E_{\mathrm{M}} - E_{\mathrm{As_4O_6}} \quad (1)$$

E(M) denotes the lithiation and magnesiation energy, E_{M} is the metallic phase energy for M atoms, and n indicates the number of atoms intercalated into the host structure. $E_{n\mathrm{M}_{\mathrm{As_4O_6}}}$ indicates the energy of the intercalated host structure, and $E_{\mathrm{As_4O_6}}$ is the energy of the pristine host.[78] The intercalation process is considered favorable only if the adsorption energy is negative, indicating an exothermic reaction. The storage capacity is a key parameter in evaluating the efficiency of anode materials for rechargeable multivalent batteries.[79,80] The storage capacity was determined based on the intercalation configurations using the following formula:

$$\text{Storage capacity} = \frac{n \times F \times z}{\mathrm{mass_{host}}} \quad (2)$$

where z denotes the valence of the Li and Mg atoms, F is Faraday's constant having a value of 26.801 A h mol^{-1},[81] $\mathrm{mass_{host}}$ is the mass of the As_4O_6 host and n indicates the number of atoms participating in the simulation.

Thermal stability analysis of the molecular cages was conducted across a range of temperatures using MD simulations. These simulations were carried out in the canonical ensemble using the Nose–Hoover thermostat (NVT). The reliability and accuracy of these simulations are ensured by selected time steps. The Climbing Image Nudged Elastic Band (CI-NEB) method was used for determining the transition states, energy barrier, diffusion pathways and reaction kinetics.[82] It enhances the maximum energy point (transition state), while all other cases have the energy at minima.[66] Six possible pathways are

assigned to each metal atom, with the one bearing the lowest energy barrier being taken as the most favorable. The force on the image is given by eqn (3):

$$F_{i\max} = |F^{s}|_{\parallel} - |\nabla E(R_{i\max})|_{\perp} \quad (3)$$

$F_{i\max}$ represents the net force on the ith image, $|\nabla E(R_{i\max})|_{\perp}$ represents the actual force and $|F^{s}|_{\parallel}$ indicates the parallel component of the spring constant.[83] The highest energy image is obtained by eqn (4).

$$R_{i\max} = \nabla E(R_{i\max}) + 2\nabla E(R_{i\max}) \quad (4)$$

The diffusion coefficient is a fundamental parameter that quantifies the diffusion mechanism within the host medium due to temperature effects.[84] Molecular dynamics simulations were performed across 300 K to 800 K using eqn (5).[3]

$$D(T) = D_0 \exp\left(-\frac{E_a}{K_B T}\right) \quad (5)$$

where $D(T)$ denotes the diffusion coefficient as a function of time, K_B is Boltzmann's constant and E_a represents the activation energy.[73] The electrochemical performance of As_4O_6 as a potential anode can be evaluated based on the open circuit voltage (OCV), which was determined by eqn (6).

$$V = \frac{E_{Mx_2As_4O_6} - E_{Mx_1As_4O_6} - (x_2 - x_1)\mu_M}{(x_2 - x_1)e} \quad (6)$$

where $E_{Mx_1As_4O_6}$ and $E_{Mx_2As_4O_6}$ are the energies of x_1 and x_2, respectively, and M represents the adsorbed metal atoms. The chemical potential of the metal atoms is represented by μ_M.[47] Ionic conductivity is a crucial parameter describing the rate of flow of intercalated ions within the host structure. The ionic conductivity is determined by eqn (7).

$$\sigma = \frac{nq^2}{K_B T} D \quad (7)$$

where q denotes the charge of the intercalated ion, D denotes the diffusion coefficient depending on temperature, T is the temperature (300 K to 900 K) and K_B is Boltzmann's constant.[83] The volume expansion is calculated by eqn (8):

$$\Delta V = \frac{V_{adsorbed} - V_{intial}}{V_{intial}} \times 100 \quad (8)$$

where $V_{adsorbed}$ is the volume of the material after adsorption and V_{intial} is the host volume of As_4O_6. Hirshfeld charge analysis was performed to examine the charge-transfer mechanism and the charge on specific atoms. This approach relies on a specific space-partitioning technique to allocate electron density among the atoms in the system.[85]

3. Results and discussions

3.1 Structural properties

In the structure of As_2O_3, the atomic orbitals combine to form molecular orbitals.[86,87] Arsenic (As) exhibits a +3 oxidation state, while oxygen (O) exhibits −2.[88] In order to complete their octet oxygen and arsenic atoms combine to form a covalent bond. However, the four As and six O atoms bond to form a cage-like structural arrangement. In molecular form, there is no direct As–As bond due to the tetrahedral arrangement of four arsenic atoms as shown in Fig. 1. This means that three O atoms surround each As atom while each O atom bridges between two As atoms creating a chemically stable, interconnected closed geometry. Bonding within As_4O_6 initially arises when the 4p orbitals of As overlap with the 2p orbitals of the O atom, leading to the formation of sigma (σ) or pi (π) molecular orbitals.[89]

The intra-cage bonding is characterized by strong covalent bonds, while the inter-cage bonding is dominated by weak van der Waals interactions.[90] This cage-like arrangement reveals the unique properties of As_4O_6, making it inert and chemically stable. The reactive sites corresponding to the dangling bonds are reduced due to the cage-like symmetry, which results in low reactivity of the material. The strain is consistently reduced by the periodic repetition within the cubic arrangement. In addition to this, strong covalent bonds exist between the oxygen and arsenic atoms, due to which they cannot easily participate in redox reactions. The electronegativity difference of the materials can easily be used to estimate the nature of chemical bonding.[91] O has an electronegativity value of 3.44, while As has a value of 2.18. The electronegativity difference between the As–As and O–O pairs is zero; as a result, the covalent character dominates within the cage. By Pauling's formula, the As–O bond shows some ionic character of 42.1%, which translates to the material. This partial ionic character reinforces the stability of cages by enhancing the electrostatic attractions within the molecular cage.[92]

First-principles calculations were employed to investigate the structural stability and parameters of pure As_4O_6-based IMCs. The formation energy of As_4O_6 is −293.90 eV which indicates that the host material is thermodynamically stable. The calculated value of the intra-atomic bonding of As–O appeared as 1.885 Å; As–As has a bond length of 3.21 Å, and O–As has a bond length of 1.885 Å, as presented in Fig. 1(a). These values are in close agreement with the reported values of 1.86 Å and 1.872 Å.[93] The interatomic distances among the atoms of different cages are 3.074 Å for O–O and 5.252 Å for As–As, as shown in Fig. 1(b). The calculated values of the dihedral bond angle within the cage are 125.6° for As–O–As, 101.5° for O–As–O, 27.9° for O–As–As and 39.3° for As–O–O. The other reported 0D inorganic molecular clusters including P_4O_6, P_4Se_3, and Sb_2O_3, exhibit similar cage-like geometries to As_4O_6.[86,94] These elements (As, P, Sb) belong to group 15 of the periodic table; as a result they exhibit similar bonding natures, chemical behaviors and oxidation states.[95] Moreover, their bond lengths and bond angles are in comparable ranges, and the presence of internal molecular gaps or voids allows the insertion and diffusion of ions.[11,86,96] These findings indicate that the molecular structure of As_2O_3 exhibit enough space, allowing the seamless insertion or removal of ions and molecules, a crucial requirement for energy storage in batteries.

3.2 Thermal stability

The thermal stability of anode materials is a critical parameter controlling the cycling reliability, safety and long-term

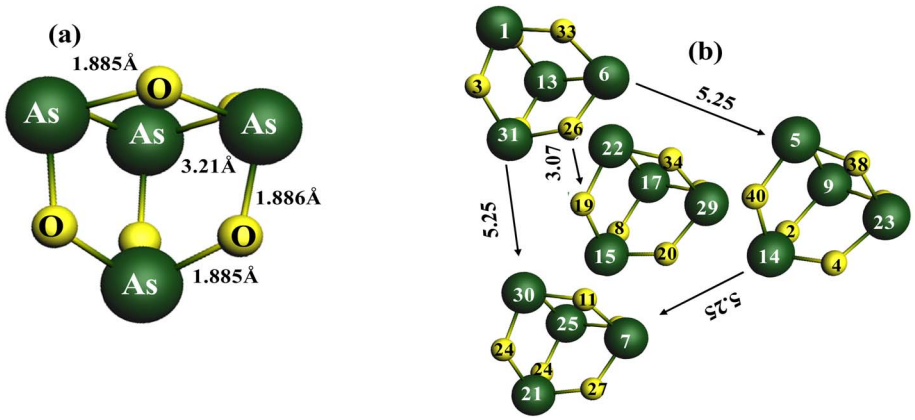

Fig. 1 Pictorial representation of (a) single cage of As_4O_6 and (b) four cages of As_4O_6.

performance of electrochemical energy-storage systems.[73] *Ab initio* molecular dynamics (AIMD) simulations were performed to determine the thermal stability of the As_4O_6 molecular cages.[97,98] These calculations were carried out using the optimized molecular cage configuration, with a total simulation time of 2500 ps and a time step of 0.25 fs. A temperature range of 300 K to 1000 K was chosen to thoroughly model the structural integrity and dynamic response of the system. These simulation findings are illustrated in Fig. 2. A structural comparison of the initial and final molecular configurations after 2500 ps at 1000 K, presented in Fig. 2(a), demonstrates the system's thermal stability. Even at this evaluated temperature, the As–O bonding remains intact, and no significant bond breakage or structural distortion occurs.

The total energy and temperature profiles over time shown in Fig. 2(b) further confirm the thermal resilience of the system. This result shares similarities with those of previously reported anode materials including P_4Se_3 IMCs, B_4C_3 and CrOCl.[76,99,100] The temperature profile fluctuates around 950–1000 K over the entire simulation trajectory, indicating that the system successfully achieved thermal equilibrium. The energy profile remains relatively stable with no signs of abrupt fluctuations that would indicate a phase transition of structural collapse.

3.3 Electronic properties of the pure As_4O_6

The electronic properties of the pure As_4O_6 were investigated to know the material's suitability for metal-ion intercalation.[101] The total density of states (TDOS) calculated for the pristine host structure presented in Fig. 3(a) indicates a band gap of 1.5 eV, indicating the semiconducting nature of the material. The TDOS further resolves into elemental contributions, as shown in Fig. 3(b), where green corresponds to the As atom and blue the O atoms. The figure clearly demonstrates that the As states exhibit a major contribution in the formation of conduction and valence bands, whereas O partially influences the valence band.

The resolved PDOS illustrated in Fig. 3(c) highlights the significant contribution of As p orbitals in the formation of the electronic structure, especially around the Fermi level. The contribution from the As s orbital is observed in the valence band, whereas the As d orbitals show negligible involvement. Fig. 3(d) reveals that the O p-orbital contributes majorly to the valence band whereas the O s and O d orbitals contribute slightly. It is concluded that the partially filled 4p-orbital of As and the 2p orbital of O are the primary drivers of the formation of valence and conduction bands as compared to the s and

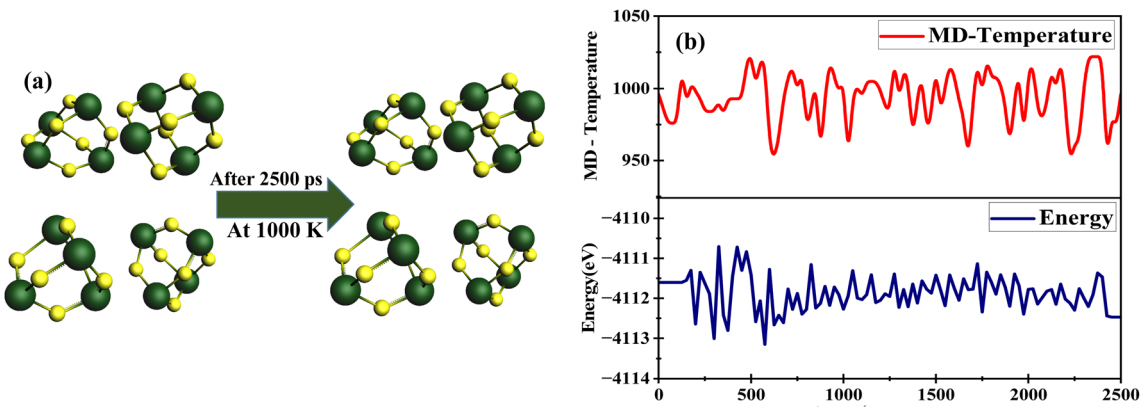

Fig. 2 (a) Snapshot of As_4O_6 before and after simulation at 1000 K, and (b) AIMD calculation showing the change in temperature and energy over time.

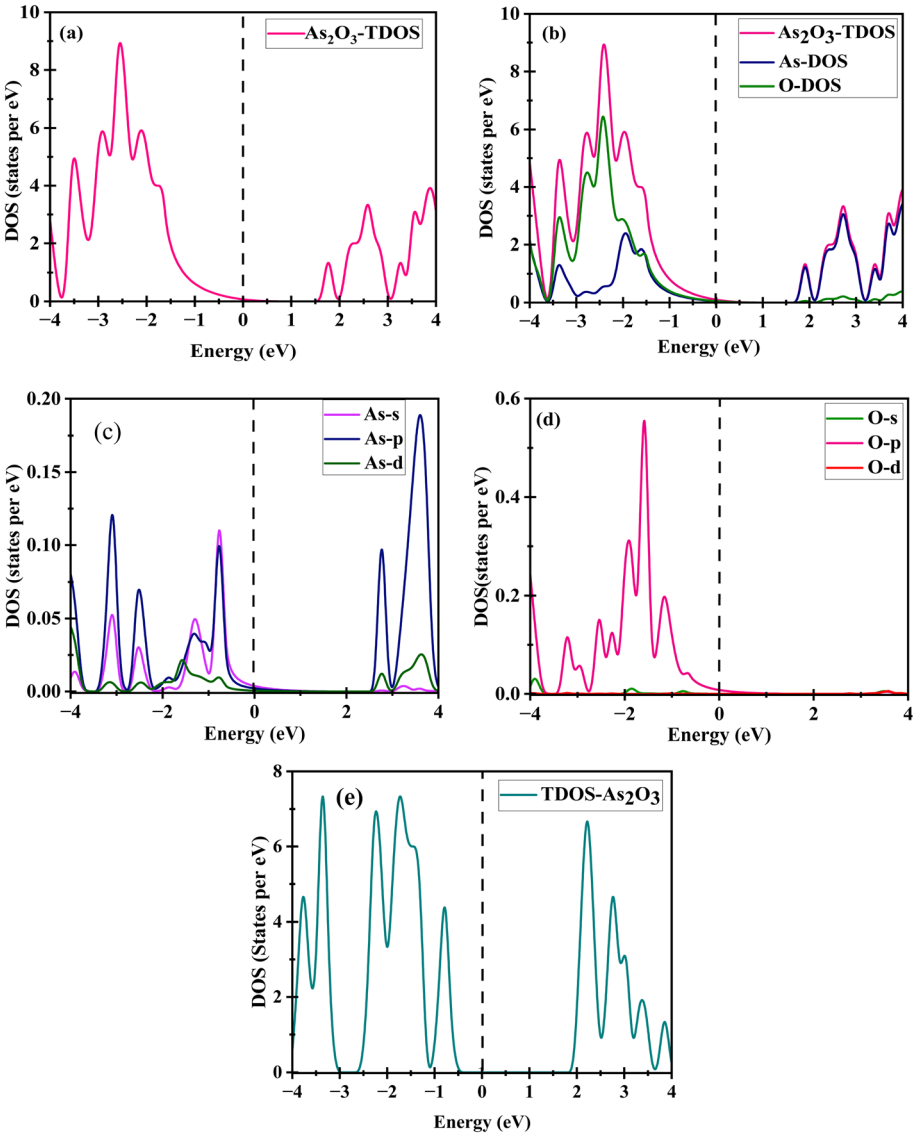

Fig. 3 (a) TDOS of the pristine As_4O_6, (b) TDOS of the As and O atoms (O), (c) PDOS of As, and (d) PDOS of the O atoms. (e) B3LYP-calculated TDOS of the pristine As_4O_6.

d orbitals. While considering the known underestimation of the band gap *via* PBE, the calculations were carried out using the B3LYP hybrid functional.[102] The As_4O_6 material shows a band gap of 2.3 eV corresponding to semiconducting behavior as shown in Fig. 1(e).

3.4 Electronic properties of As_4O_6 upon intercalation

DOS analysis was performed to examine the electronic behavior of the As_4O_6 molecular cages and their interaction between the intercalated Li and Mg metal atoms.[73,103] DOS calculations were conducted for both the pristine and intercalated host structures. The introduction of metal atoms influences the electronic conductivity of the host material. The TDOS for the Li-intercalated system reveals a notable change in the electronic behavior of the pristine host structure, as shown in Fig. 4(a). The TDOS of the Li-intercalated As_4O_6 system is shown in pink, while the DOSs of As, O and Li are highlighted in blue, green and red, respectively. The TDOS upon intercalation exhibits non-zero and substantial density of states at the Fermi level, signifying a marked transition from semiconducting to metallic characteristics. The complete disappearance of the band gap observed in the Li-intercalated system allows the free movement of charge carriers, resulting in a significant enhancement in electrical conductivity.

The s-orbital of Li interacts with the p orbitals of As and O. The Li 2s state interacts with the pure As_4O_6 electronic states transferring their charge to the host structure. During Li intercalation, near the Fermi level, there is a significant increase in peaks in the conduction bands. This shows that the electrical conductivity improves and notable reduction in the band gap of the host material occurs.

Mg intercalation also results in comparable modification. The TDOS for the Mg-intercalated host structure is represented

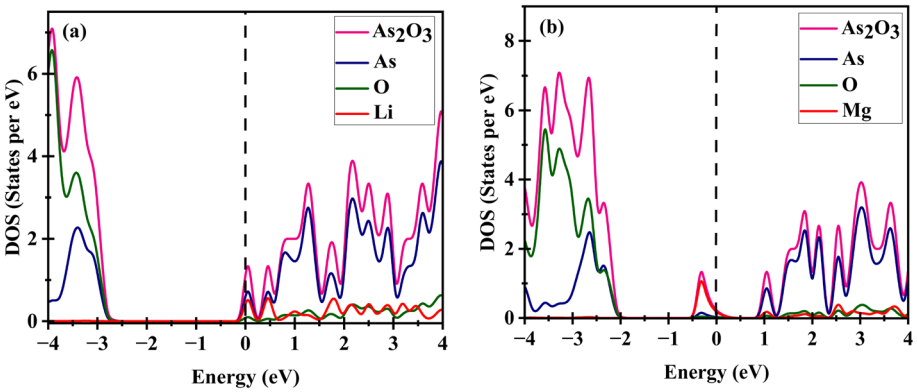

Fig. 4 Calculated DOSs of As_4O_6 after (a) one Li intercalation and (b) one Mg intercalation.

by a pink curve in Fig. 4(b), with the DOSs of As, O and Mg highlighted in blue, green and red curves, respectively. The TDOS for the Mg-intercalated host structure also shows continuous density of states at the Fermi level, resulting in the elimination of the band gap and the transition to metallic properties that enhance conductivity. The elemental contributions reveal a strong contribution from Mg directly at the Fermi level, as illustrated in Fig. 4(b), indicating prominent electron donation. The Mg s states interact strongly with the As-dominated states, facilitating charge transfer from Mg to the host structure. It is concluded that the pristine As_4O_6 structure is an intrinsic semiconductor with a band gap of 1.5 eV. However, upon intercalation, its properties drastically change with the elimination of the band gap, inducing the metallic behavior of the host system.

3.5 Favorable intercalation sites

Identifying energetically favorable intercalation sites is pivotal for determining the ion storage mechanism and predicting the performance of anode materials.[104] Favorable intercalation sites are the sites where the ions face the minimum energy barrier when intercalated within the host material. The more negative the energy values, the more favorable the exothermic reaction, demonstrating the validity of the host as a viable anode material.[105,106] In this work, Li and Mg atoms are positioned at various sites in the As_4O_6 molecular cages, and their energy profiles were examined. The intercalation energy was calculated *via* eqn (1), with the Li and Mg atoms placed at different intercalation sites.

Direct intercalation within the As_4O_6 molecular cages was not energetically favorable due to structural inertness. This research mainly focused on the external adsorption sites. However, the Li atoms positioned at A1 and A2 sites near the O atoms, as illustrated in Fig. 5, show the minimum energy profile compared with the atoms at other sites. These sites yielded the minimum energy profile, with an appropriate intercalation energy of −7.12 eV. Similarly, Mg offered a minimum intercalation energy of −1.46 eV when intercalated at sites A1 and A2. The most favorable sites are near the O atoms, which have a higher electron affinity and electronegativity than the As atoms, facilitating more effective charge transfer and electrostatic interaction from the intercalating ions.

3.6 Intercalation energies of the adsorbed guest atoms

The identification of effective anode materials possessing high storage capacity, structural stability and thermodynamically favorable intercalation energies is a key challenge in the development of high-performance metal-ion batteries.[107] For this purpose, we comprehensively investigated the adsorption energies of the As_4O_6 host structure intercalated with metal atoms. Our approach involved the sequential addition of metal atoms and the measurement of the energy profile to identify the saturation limit at which the process makes a transition from exothermic to endothermic. When an atom is intercalated with a host material, the value of the intercalation energy tells whether the process is endothermic or exothermic (favorable).[99,108] The negative intercalation energy points to a favorable process, indicating that more M atoms can be intercalated within the As_4O_6 host structure.

Eqn (1) is utilized to calculate the value of the adsorption energy. To evaluate the intercalation process, the concentration of M atoms was gradually increased. After the intercalation of the atoms one by one, if the adsorption energy remains negative, more metal atoms can be adsorbed stably. The total number of atoms intercalated before the reaction shifts is utilized in eqn (2) for calculating the theoretical storage capacity. For LIBs, our results show that the theoretical capacity

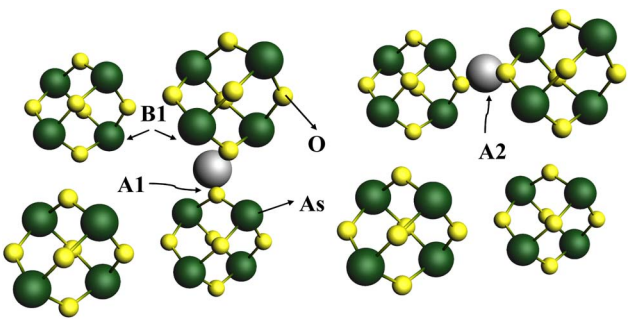

Fig. 5 Favorable intercalation sites for LIBs and MIBs.

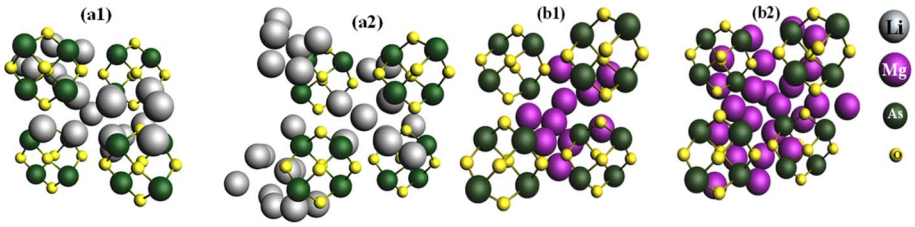

Fig. 6 Optimized structure of As_4O_6 with (a1) 10 Li atoms, (a2) 27 Li atoms, (b1) 10 Mg atoms and (b2) 30 Mg atoms.

for Li storage, with sequential insertion into the host structure, is up to 27 Li atoms, for which the reaction remains exothermic. Beyond this, the 28th Li-atom insertion shifts the reaction to an endothermic process. The blue line in Fig. 7 presents the concentration-dependent energy profile of Li atoms for LIBs. The optimized structures of the As_4O_6 molecular cages with 10 and 27 intercalated Li atoms are shown in Fig. 6(a1) and (a2), respectively.

Similarly, for MIBs, the Mg atoms are sequentially inserted into the cage structures, and the reaction remains exothermic until the 30th atom. After this saturation point, the process shifts toward the endothermic regime as shown in Fig. 7, where the red line shows the intercalation energy profile for the MIBs. The optimized structures of the As_4O_6 molecular cages with 10 and 30 intercalated Mg atoms are shown in Fig. 6(b1) and (b2), respectively.

3.7 Storage capacity

The calculation of the storage capacity is crucial for the development of anode materials to be used in LIBS and MIBs.[109] Eqn (2) determines the theoretical storage capacity of As_4O_6 as an anode material for both LIBs and MIBs under exothermic reaction conditions. The exothermic regime continues until the intercalation of the maximum number of metal atoms, signifying a thermodynamically favorable process. The saturation point was described in Section 3.6 as 27 atoms for Li and 30 for Mg. The theoretical reversible capacity computed for LIBs is 457.21 mA h g^{-1}, while the intercalation process remains exothermic for up to 27 Li atoms, as presented in Fig. 8(a). This modest capacity is still higher than that of reported low-dimensional materials, such as Co_9S_8 cage-like microspheres (303.5 mA h g^{-1}) and LiC_6 (372 mA h g^{-1}), indicating that As_4O_6 exhibits a competitive storage capacity for LIB applications.[56,110] In contrast, As_4O_6 exhibits a theoretical reversible capacity of 1016 mA h g^{-1} for MIBs, as shown in Fig. 8(b), which is the highest value among all battery systems in this study. This value is significantly higher than those of other reported materials, such as P_4Se_3 molecular cages (519 mA h g^{-1}), Bi nanotubes (303 mA h g^{-1}), Mg_3Bi_2 nanocluster (263 mA h g^{-1}) and MoS_2 (469 mA h g^{-1}), confirming its suitability for MIBs.[57,58,90,99] This simulation indicates that the theoretical capacity of the MIBs is twice that of the LIBs, as the As_4O_6 molecular cages have the ability to hold a greater number of magnesium atoms than lithium, as shown in Fig. 8.

The capacity of the MIBs is approximately double those of the LIBs, making As_4O_6 a promising anode material for batteries. The high theoretical capacity of the MIBs supports the validity of using As_4O_6 as an anode material; however, its performance in LIBs is limited due to the low storage capacity. The intrinsic thermal stability and structural stability, along with the theoretical capacity, position As_4O_6 as a promising anode for use in advanced energy-storage applications.

3.8 Diffusion pathways

The overall electrochemical performance of a battery crucially depends on the energy barriers encountered by metal ions as they migrate through the anode host structure.[111] These barriers correspond to the resistance that ions experience during intercalation and directly influence the efficiency of the discharging–charging process, ultimately affecting the battery's cycling stability and rate capacity.[112,113] For this purpose, CI-NEB simulations were carried out to identify the migration pathways and their corresponding energy barriers for the intercalated metal atoms within the As_4O_6 host. Six different pathways were initially investigated for each guest metal atom in the As_4O_6 host, whereas the pathways corresponding to the minimum energy barrier are reported here. The energy is calculated as the energy difference between the transition and initial states encountered by metal atoms during the process of intercalation. For LIBs, several diffusion pathways were studied to evaluate the Li-ion transport within the As_4O_6 framework, as presented in Fig. 9(a)and (b). Fig. 9(a) displays the most

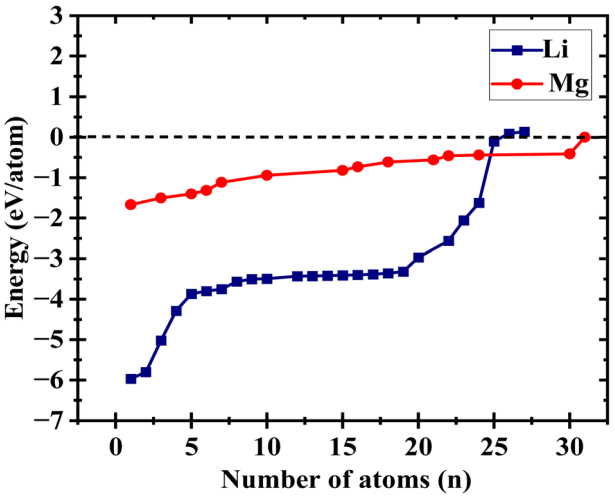

Fig. 7 Intercalation energy of the pure As_4O_6 host with Li and Mg atoms as a function of concentration.

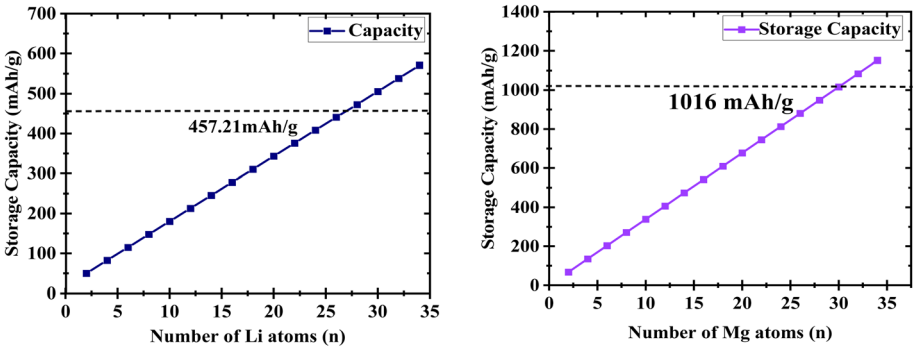

Fig. 8 Calculated storage capacities of (Left) LIBs and (Right) MIBs.

favorable migration route for Mg ions. Along this path, the calculated energy barrier is 0.77 eV along the *x*-axis and 0.35 eV along the *y*-axis, indicating the reaction kinetics of Mg from left to right. Similarly, six diffusion paths were investigated for Mg intercalation in the As_4O_6 host structure. The most favorable diffusion path for the Mg intercalation along the *x*-axis is illustrated in Fig. 9(a). This pathway has the lowest energy barrier of all paths investigated, *i.e.*, 0.52 eV. Fig. 9(b) illustrates the most favorable diffusion path for Mg along the *y*-axis that exhibits a low energy barrier of 0.13 eV. It implies that 0.13 eV energy is required for Mg to overcome this resistance and intercalate into the host structure.[114]

The comparison with established anode materials indicates the following: graphite exhibits a theoretical capacity of 372 mA h g^{-1} with a diffusion barrier of around 0.3–0.4 eV, P_4Se_3 IMCs (519 mA h g^{-1} for MIBs) experience an energy barrier of 0.30 eV, B_4C_3 (2770 mA h g^{-1} for LIBs) experiences an energy barrier around 0.20–0.25 eV, Mo_6S_8 (469 mA h g^{-1} for MIBs) experiences an energy barrier of 0.4–0.6 eV, and TiO_2 (110 mA h g^{-1}) experiences an energy barrier around 0.63 eV.[8,42,76,100,115] Some other traditional anode materials, like silicon and Sn-based materials, provide a stable, high storage capacity, but they are known to suffer from sluggish ion diffusion and volume expansion.[116,117] The comparative analysis indicates the worth of our proposed material when performance metrics, including storage capacity and cycling stability, are taken into account. An energy barrier less than 1 eV is considered favorable for ion diffusion in anode materials.[3] These low

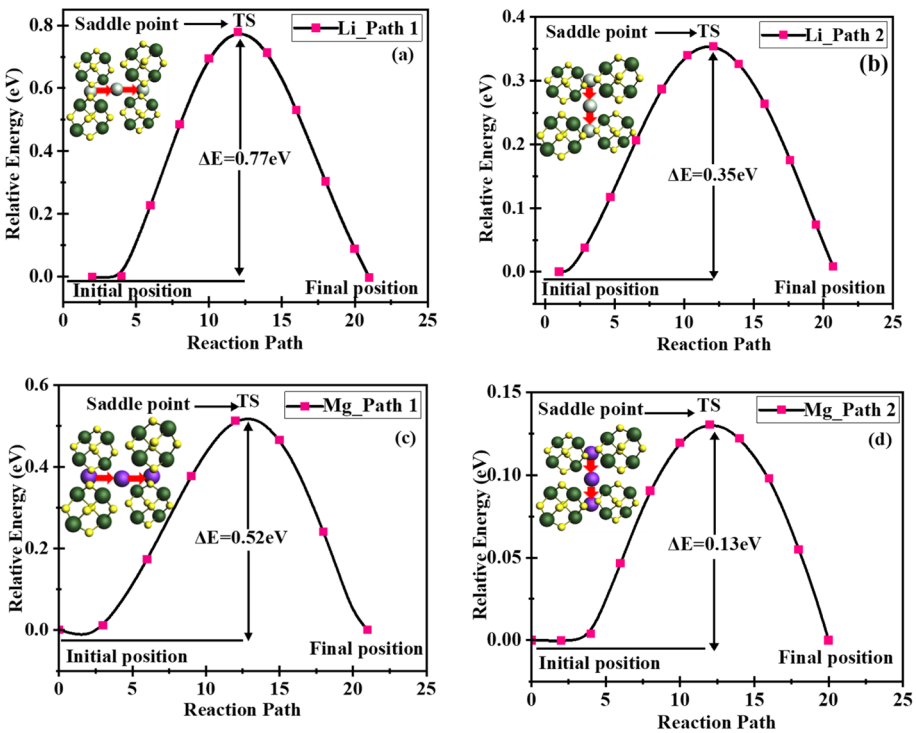

Fig. 9 Minimum energy barrier encountered by (a) Li atoms along the *x*-axis, (b) Li atoms along the *y*-axis, (c) Mg atoms along the *x*-axis and (d) Mg atoms along the *y*-axis.

energy barriers suggest fast ion transport, which enhances cycling stability and contributes to excellent rate performance, thereby confirming As_4O_6's suitability as a high-performance anode material.

3.9 Stability of fully loaded structures

AIMD calculations were conducted on the fully loaded As_4O_6 molecular cages to assess the feasibility of the capacity predictions and the structural stability at a temperature of 500 K. These simulations were performed for 2.5 ps, and each step had a temporal duration of 0.25 fs. Both LIBs and MIBs were considered in this study, with the host structure fully loaded with intercalated ions. In the case of LIBs, 27 Li atoms are intercalated in the host structure, as shown in Fig. 10(a), and 30 Mg atoms are intercalated in the host for MIBs, as shown in Fig. 10(d). The variations in the energy and temperature profiles over time for both fully loaded systems are shown in Fig. 10. This implies that the energy of the loaded system shows a gradual decrease over time due to the atomic rearrangement that minimizes internal stress. This energy eventually stabilizes as the system relaxes, indicating that the system has achieved the equilibrium state.[117,118]

Moreover, the temperature remains stable for both systems, fluctuating around a constant mean value.[119] This behavior confirms that both systems have attained thermal equilibrium and that the energy exchange between the particles has stabilized over time. The absence of any bond breakage, as visualized in Fig. 10, indicates that the system maintains its structural integrity over intercalation. The preserved pristine host framework, coupled with the system's temperature-energy profile, as illustrated in Fig. 2, further supports its suitability and validity for energy-storage devices.

3.10 Diffusion coefficient of As_4O_6

The diffusion coefficient of the intercalating metal ions in the host structure plays a vital role in determining the performance and effectiveness of anode materials in energy-storage devices.[120] It directly affects the battery's energy density, cycling stability and overall electrochemical performance. This parameter governs how quickly metal ions migrate through the anode material during discharging or charging cycles. Molecular dynamics (MD) simulations were conducted over a broad temperature range of 300 K to 900 K in order to understand this behavior. These simulations shed light on the ion transport within the host structure and characterized the temperature-dependent behavior of ion diffusivity.

Fig. 11 illustrates the ion transport phenomenon using an Arrhenius plot constructed from the calculated values of the diffusion coefficient. In this research, the diffusion coefficients for both the LIBs and MIBs were calculated. The calculated diffusion coefficient for the LIBs is 1.09×10^{-7} m^2 s^{-1}, as shown in Fig. 11(a) and (b) shows the calculated diffusion coefficient for the MIBs as 1.13×10^{-7} m^2 s^{-1}. This implies that the diffusion coefficients for the LIBs and MIBs are nearly identical, only slightly higher for the MIBs.

3.11 Ionic conductivity of As_4O_6

Ionic conductivity is a significant property that directly evaluates the ion-transport efficiency and profoundly influences the overall performance of metal-ion batteries.[120–122] Materials with a high ionic conductivity facilitate faster ion migration during charging and discharging processes, which influences high power output and extended cycle life. The temperature-dependent mobility of Li and Mg ions within the As_4O_6 host

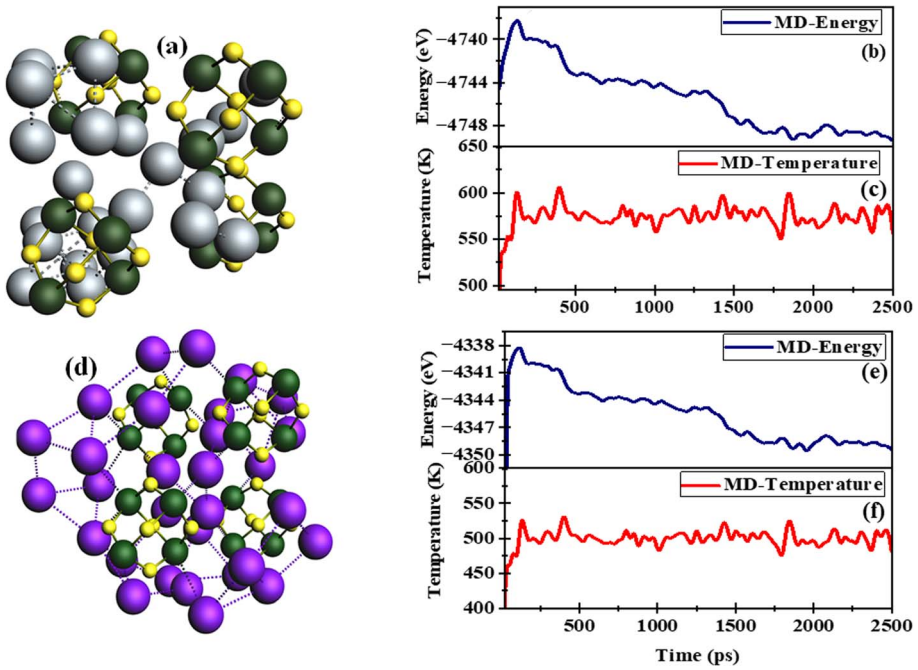

Fig. 10 Energy and temperature profiles of the fully loaded structures over time at 500 K for (a–c) LIBs and (d–f) MIBs.

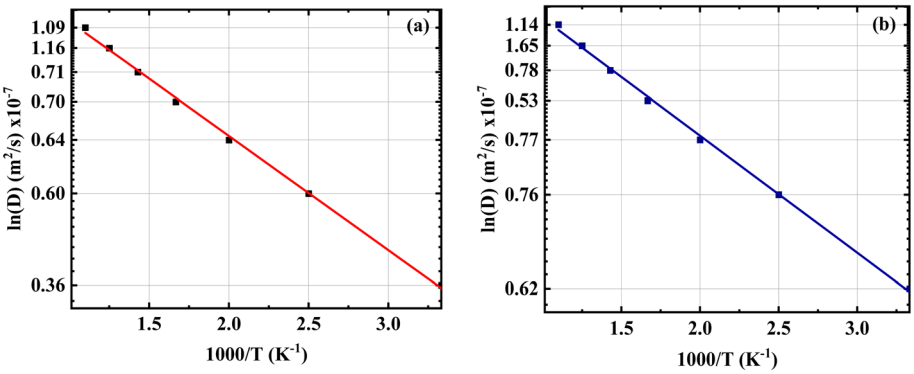

Fig. 11 Calculated diffusion coefficients for (a) LIBs and (b) MIBs.

was investigated, with the results displayed in Fig. 12. The ionic conductivity for the LIBs as a function of temperature is illustrated in Fig. 12(a). At 300 K, the LIBs exhibit an ionic conductivity of 1.05×10^{-7} S m^{-1}, while the MIBs demonstrate an ionic conductivity of 2.05×10^{-7} S m^{-1} under the same operating conditions, as illustrated in Fig. 12(b). The ionic conductivity consistently increases with temperature over the study range of 300 K to 800 K. The ionic conductivity for the Mg-ion transport is indeed higher than that for the Li-transport in the host structure. The calculated ionic conductivity values remain consistent at approximately 10^{-7} S m^{-1} across the evaluated temperature ranges, which typically falls within the frequently reported ranges for solid electrode materials.[123] These results align with the low energy barriers as reported in Section 3.9 indicating that As_4O_6 possesses sufficient ionic conductivity to support effective ion transport under the operating conditions.

These results align with the low energy barriers as reported in earlier Section 3.9, indicating that As_4O_6 possesses sufficient ionic conductivity to support effective ion transport under operating conditions.

3.12 Voltage profiling of As_4O_6

The open circuit voltage (OCV) is a defining parameter for energy-storage technologies.[58,124,125] It serves as a fundamental parameter to determine the overall performance of the battery and the charge state.[121] In the context of multivalent batteries, their electrochemical performance is based on the OCV of the anode materials as it directly influences the charge–discharge voltage profile, achievable charge density and thermodynamic stability. It is directly linked to the theoretical capacity because, as the ion intercalates into the host structure, the battery's theoretical capacity increases while the potential difference between the electrodes of the battery typically decreases. The voltage profile of the As_4O_6 molecular cages for LIBs, shown in Fig. 13(a), illustrates the trend of OCV with ion concentration (n). For LIBs, as the number of lithium ions increases, the voltage profile gradually decreases from a high initial value of 5.97 V to 0.66 V, indicating that the OCV stabilizes at 0.66 V. The voltage profile for the MIBs, shown in Fig. 13(b), demonstrates that as the concentration of Mg ions increases, the voltage difference between electrodes continuously decreases. The OCV for the MIBs starts from 1.46 to 0.23 V, consistent with expected values for stable systems. The As_4O_6 IMCs show lower intercalation voltages (0.23 V for Li and 0.66 for Mg) compared to the other 0D materials, such as C_{60} (0.6–0.8 V) and Co_3O_4 QDs (0.9 V).[49,101,102]

The anode materials having a voltage range of 0.1 to 1 V are generally considered electrochemically stable.[103] In this work, the stability of As_4O_6 as a potential anode material for LIBs and MIBs is confirmed by the voltage values of 0.66 V and 0.23 V. These results highlight the material's potential for effective energy-storage applications.

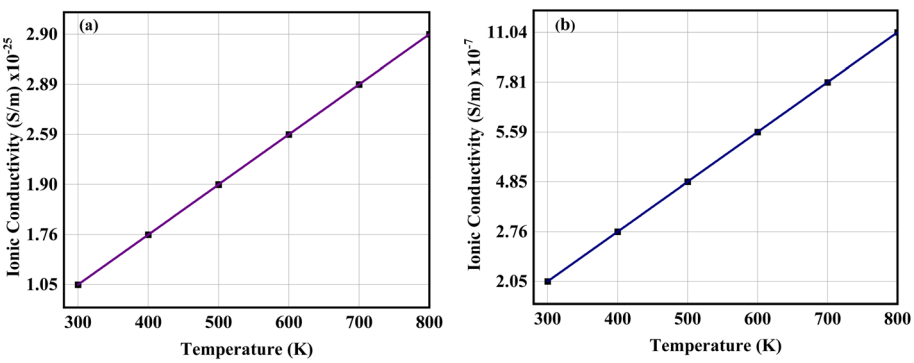

Fig. 12 Calculated ionic conductivity as a function of temperature for (a) LIBs and (b) MIBs.

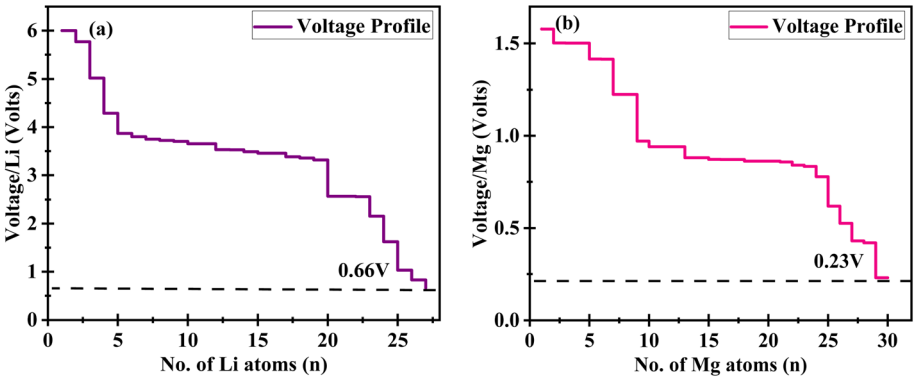

Fig. 13 Calculated voltage profile of the (a) Li-intercalated and (b) Mg-intercalated As_4O_6 structure.

3.13 Volume expansion

The structural stability of the molecular cages is an essential parameter when utilizing them as anode materials for metal-ion batteries. A key indicator of the stability is the degree of volume expansion during ion adsorption as the capacity starts fading when considerable volume expansion takes place.[126] To quantify this effect, we applied the bounding-sphere method, which defines the effective cage radius R as the maximum distance between the mass-weighted center of mass (COM) and any atomic coordinate in the optimized structure; the volume expansion was calculated using eqn (8). For the pristine As_4O_6 molecular cage, the calculated bounding-sphere radius was $R =$ 6.418 Å, and the calculated effective volume was 1107.6 Å^3. Firstly, 27 Li atoms are adsorbed, and the radius value slightly changes to 6.451 Å, which corresponds to a volume expansion of 1.54%. Similarly, for Mg the radius also changes slightly to 6.452 Å, and the effective volume is 1125.1 Å^3. Mg adsorption produced a comparable cage/volume expansion of 1.57%, which proves the structural rigidity of the host framework even under multivalent ion insertion. Such minimal expansion (<2%) is significantly lower than those reported for alloy-type or conversion-type anodes, which often undergo volume changes exceeding 200–300% (*e.g.*, Si, Sn, or P-based systems).[127] Even compared to nanostructured transition-metal oxides, which typically show 10–30% expansion, the As_4O_6 molecular cage demonstrates mechanical robustness.[128] These results strongly suggest that the As_4O_6 cage structure is capable of maintaining cycling stability without major morphological degradation.

The bounding-sphere method has been previously adopted for 0D nanostructures and clusters to evaluate geometric stability, particularly where conventional lattice-based volume measures are not applicable.[102,127–129] Our results confirm that such cage-type 0D anode materials can deliver a high theoretical capacity with minimal volumetric distortion, making them competitive alternatives to conventional layered or alloy-based anodes.

3.14 Hirshfeld charge analysis

Understanding the charge transfer between the host structure and intercalated metal ions is essential for comprehending the electrochemical mechanism that governs ion intercalation in rechargeable batteries.[130] Hirshfeld charge analysis was employed to investigate the charge distribution between the host materials and intercalated metal atoms, which is necessary for enhancing battery performance.[49] Fig. 14 presents the Hirshfeld charge analysis, with the color scale identifying the magnitude of local charges. The initial analysis of the pristine As_4O_6, as presented in Fig. 14(a), reveals that the red color signifies minor charges, while the blue denotes the major charge. This indicates that the O atom carries a positive charge, while As offers a negative charge and the charge is inherently transferred from oxygen to arsenic atoms. Furthermore, the charge is predominantly localized within the single cage, and there is negligible charge density between cages.

This suggests that there is no strong binding between the inter-cage, validating the fact that cages are inert and have no

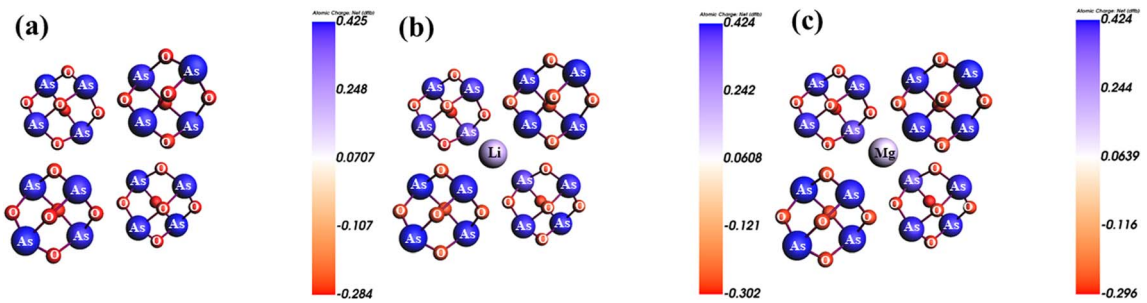

Fig. 14 Hirshfeld charge analysis for As_4O_6: (a) pristine, (b) single Li-intercalated, and (c) single Mg-intercalated configurations.

fundamental forces between them.[86] The charge transfers between the Li-intercalated and As_4O_6 molecular cages are effectively visualized in Fig. 14(b). The host atom exhibits the major charge, while the Li atom exhibits the minor charge. Similarly, upon Mg intercalation a significant increase in the electron density of the host material is observed as shown in Fig. 14(c). This implies that the electron density transfers to the host material rather than Mg during intercalation. This suggested that enhanced charge accumulation on the host material leads to better electronic conductivity and more stable charge distribution.

4. Summary

DFT calculations were carried out to explore the potential of As_4O_6 molecular cages as an anode material for monovalent and multivalent ion batteries. The calculations were conducted to investigate the electronic properties, alongside the charge-transfer mechanisms, redox properties, storage capacity and electrochemical performance. Molecular dynamics simulation under electrochemical conditions confirmed the structural stability of the host structure, demonstrating its suitability for use in next-generation batteries. AIMD simulation confirmed the system theoretical stability upon intercalation with magnesium and lithium atoms, making it a promising material for rechargeable batteries. This research highlights the critical aspects of ion diffusion, adsorption and reaction kinetics, demonstrating the material's suitability for durable high-capacity anode applications. The evaluated theoretical capacities of the LIBs and MIBs reached 457 mA h g^{-1} and 1012 mA h g^{-1}, respectively. This investigation highlights that the battery performance can be enhanced by the exothermic interaction between the host material and the intercalated ion. The calculated values of the diffusion coefficient were 1.09×10^{-7} m^2 s^{-1} for the LIBs and 1.13×10^{-7} m^2 s^{-1} for the MIBs. CI-NEB simulations determined the minimum energy barrier to be 0.35 eV for LIBs and 0.13 eV for MIBs, revealing the fast ion mobility and diffusion properties of As_4O_6 IMCs. The OCV analysis indicated that as the concentration of Li ions increases, the voltage profile gradually decreases from 5.97 V to 0.66 V indicating that the OCV stabilizes at 0.66 V while for the MIBs it starts from 1.46 V to 0.23 V. From the perspective of computational parameters, as well as toxicity of the material, an extensive evaluation of As_4O_6 was carried out. The present knowledge further strengthens its viability as a fast-diffusing, high-capacity anode for Li-ion and Mg-ion batteries. The findings demonstrate that As_4O_6 molecular cages represent an appealing battery technology option because they deliver outstanding capacity performance, together with swift ion transport and sustained electrochemical behavior. This study plays a vital role in advancing zero-dimensional anode materials, serving as the basis for developing improvement methods for energy storage systems.

Conflicts of interest

The authors declare that they have no known competing financial interests or personal relationships that could have appeared to influence the work reported in this paper.

Data availability

The code for the Amsterdam Density Functional (ADF) can be found at **https://www.scm.com**. The version of the code employed for this study is 2022.[131]

Acknowledgements

The authors extend their appreciation to the King Saud University, Saudi Arabia, for funding this work through the Ongoing Research Funding Program, (ORF-2025-993), King Saud University, Riyadh, Saudi Arabia.

References

1 G. Lovat, B. Choi, D. W. Paley, M. L. Steigerwald, L. Venkataraman and X. Roy, Room-temperature current blockade in atomically defined single-cluster junctions, *Nat. Nanotechnol.*, 2017, **12**(11), 1050–1054, DOI: **10.1038/nnano.2017.156**.
2 A. Majid and M. Bibi, *Cadmium based II-VI semiconducting nanomaterials*, Gewerbestrasse, 2018, vol. 11, p. 6330.
3 P. Canepa, *et al.*, Odyssey of Multivalent Cathode Materials: Open Questions and Future Challenges, *Chem. Rev.*, 2017, **117**(5), 4287–4341, DOI: **10.1021/acs.chemrev.6b00614**.
4 A. Jamal, M. S. H. Faizi and N. Dege, Synthesis, Structural Characterization, DFT Calculations, and Molecular Docking of a Novel Quinoline Derivative, *J. Mol. Struct.*, 2024, **1300**, 137251, DOI: **10.1016/j.molstruc.2023.137251**.
5 W. Han, *et al.*, Two-Dimensional Inorganic Molecular Crystals, *Nat. Commun.*, 2019, **10**, 4728.
6 M. Cinchetti, V. A. Dediu and L. E. Hueso, Activating the molecular spinterface, *Nat. Mater.*, 2017, **16**(5), 507–515, DOI: **10.1038/nmat4902**.
7 K. Liu, L. Liu and T. Zhai, Emerging Two-Dimensional Inorganic Molecular Crystals: The Concept and Beyond, *J. Phys. Chem. Lett.*, 2022, **13**(9), 2173–2179, DOI: **10.1021/acs.jpclett.1c04213**.
8 J. M. Buriak, Up-and-Coming Perspectives: Share the Excitement of Top Early Career Researchers in Materials Chemistry, *Chem. Mater.*, 2016, **28**(12), 4083–4084, DOI: **10.1021/acs.chemmater.6b02242**.
9 X. Feng, *et al.*, Effect of Strong Intermolecular Interaction in 2D Inorganic Molecular Crystals, *J. Am. Chem. Soc.*, 2021, **143**(48), 20192–20201, DOI: **10.1021/jacs.1c08030**.
10 L. Cronin, Inorganic molecular capsules: from structure to function, *Angew. Chem., Int. Ed.*, 2006, **45**(22), 3576–3578.
11 Y. Cao, *et al.*, P4Se3 as a new anode material for sodium-ion batteries, *J. Alloys Compd.*, 2019, **775**, 1286–1292, DOI: **10.1016/j.jallcom.2018.10.215**.
12 A. Majid, N. Z. Raza, S. Ahmad and M. Alkhedher, Electrochemical Performance of P4Se3 as High-Capacity Anode Materials for Monovalent and Multivalent Ion Batteries, *Mater. Chem. Phys.*, 2024, 129515.
13 J. L. Rose, T. C. VanCott, P. N. Schatz, M. E. Boyle and M. H. Palmer, Vacuum ultraviolet spectroscopy of

Group V oxides: P4O6 and As4O6, *J. Phys. Chem.*, 1989, **93**(9), 3504–3511.
14 B. Dunn, H. Kamath and J.-M. Tarascon, Electrical energy storage for the grid: a battery of choices, *Science*, 2011, **334**(6058), 928–935.
15 K. H. Solangi, M. R. Islam, R. Saidur, N. A. Rahim and H. Fayaz, A review on global solar energy policy, *Renew. Sustain. Energy Rev.*, 2011, **15**(4), 2149–2163, DOI: 10.1016/j.rser.2011.01.007.
16 Y. Wang, H. Kwok, W. Pan, H. Zhang and D. Y. Leung, Innovative paper-based Al-air batteries as a low-cost and green energy technology for the miniwatt market, *J. Power Sources*, 2019, **414**, 278–282.
17 S. R. Salkuti, Emerging and advanced green energy technologies for sustainable and resilient future grid, *Energies*, 2022, **15**, 6667.
18 K. Osmani, *et al.*, Recent progress in the thermal management of lithium-ion batteries, *J. Clean. Prod.*, 2023, **389**, 136024, DOI: 10.1016/j.jclepro.2023.136024.
19 A. Midilli, I. Dincer and M. Ay, Green energy strategies for sustainable development, *Energy Policy*, 2006, **34**(18), 3623–3633, DOI: 10.1016/j.enpol.2005.08.003.
20 J.-M. Tarascon and M. Armand, Issues and challenges facing rechargeable lithium batteries, *Nature*, 2001, **414**(6861), 359–367.
21 P. Gu, M. Zheng, Q. Zhao, X. Xiao, H. Xue and H. Pang, Rechargeable zinc–air batteries: a promising way to green energy, *J. Mater. Chem. A*, 2017, **5**(17), 7651–7666.
22 S. Duehnen, J. Betz, M. Kolek, R. Schmuch, M. Winter and T. Placke, Toward green battery cells: perspective on materials and technologies, *Small Methods*, 2020, **4**(7), 2000039.
23 M. S. Whittingham, Lithium Batteries and Cathode Materials, *Chem. Rev.*, 2004, **104**(10), 4271–4302, DOI: 10.1021/cr020731c.
24 Y. Miao, P. Hynan, A. Von Jouanne and A. Yokochi, Current Li-ion battery technologies in electric vehicles and opportunities for advancements, *Energies*, 2019, **12**(6), 1074.
25 J. M. Tarascon and M. Armand, Issues and challenges facing rechargeable lithium batteries, *Nature*, 2001, **414**(6861), 359–367, DOI: 10.1038/35104644.
26 M. M. Thackeray, C. Wolverton and E. D. Isaacs, Electrical energy storage for transportation—approaching the limits of, and going beyond, lithium-ion batteries, *Energy Environ. Sci.*, 2012, **5**(7), 7854–7863.
27 M. J. Lain and E. Kendrick, Understanding the limitations of lithium ion batteries at high rates, *J. Power Sources*, 2021, **493**, 229690.
28 A. Mahmood, *et al.*, Enabling high-performance multivalent metal-ion batteries: current advances and future prospects, *Chem. Soc. Rev.*, 2025, **54**(5), 2369–2435, DOI: 10.1039/D4CS00929K.
29 D. Larcher and J.-M. Tarascon, Towards greener and more sustainable batteries for electrical energy storage, *Nat. Chem.*, 2015, **7**(1), 19–29.
30 D. Di Lecce, R. Verrelli and J. Hassoun, Lithium-ion batteries for sustainable energy storage: recent advances towards new cell configurations, *Green Chem.*, 2017, **19**(15), 3442–3467.
31 R. Shah, V. Mittal, E. Matsil and A. Rosenkranz, Magnesium-Ion Batteries for Electric Vehicles – Current Trends and Future Perspectives, *Adv. Mech. Eng.*, 2021, **13**(3), DOI: 10.1177/16878140211003398.
32 R. Dominko, J. Bitenc, R. Berthelot, M. Gauthier, G. Pagot and V. Di Noto, Magnesium batteries: current picture and missing pieces of the puzzle, *J. Power Sources*, 2020, **478**, 229027, DOI: 10.1016/j.jpowsour.2020.229027.
33 H. D. Yoo, I. Shterenberg, Y. Gofer, G. Gershinsky, N. Pour and D. Aurbach, Mg rechargeable batteries: an on-going challenge, *Energy Environ. Sci.*, 2013, **6**(8), 2265–2279.
34 H. E. Friedrich and B. L. Mordike, *Magnesium Technology*, Springer, 2006.
35 X. Yuan, H. Liu and J. Zhang, *Lithium-Ion Batteries: Advanced Materials and Technologies*, CRC Press, 2011.
36 M. R. Raj, G. Lee, M. V. Reddy and K. Zaghib, Recent Advances in Development of Organic Battery Materials for Monovalent and Multivalent Metal-Ion Rechargeable Batteries, *ACS Appl. Energy Mater.*, 2024, **7**(19), 8196–8255, DOI: 10.1021/acsaem.3c02382.
37 W.-J. Zhang, A review of the electrochemical performance of alloy anodes for lithium-ion batteries, *J. Power Sources*, 2011, **196**(1), 13–24.
38 D. Di Lecce, *et al.*, Multiwalled Carbon Nanotubes Anode in Lithium-Ion Battery with LiCoO2, Li[Ni1/3Co1/3Mn1/3]O2, and LiFe1/4Mn1/2Co1/4PO4 Cathodes, *ACS Sustain. Chem. Eng.*, 2018, **6**(3), 3225–3232, DOI: 10.1021/acssuschemeng.7b03395.
39 R. Shah, V. Mittal, E. Matsil and A. Rosenkranz, Magnesium-ion batteries for electric vehicles: current trends and future perspectives, *Adv. Mech. Eng.*, 2021, **13**(3), DOI: 10.1177/16878140211003398.
40 F. Wang, *et al.*, High-voltage aqueous magnesium ion batteries, *ACS Cent. Sci.*, 2017, **3**(10), 1121–1128.
41 X. Su, *et al.*, Silicon-Based Nanomaterials for Lithium-Ion Batteries: A Review, *Adv. Energy Mater.*, 2014, **4**(1), 1300882, DOI: 10.1002/aenm.201300882.
42 E. Feyzi, K. Anil, X. Lia, S. Deng, J. Nanda and K. Zaghib, A comprehensive review of silicon anodes for high-energy lithium-ion batteries: challenges, latest developments, and perspectives, *Next Energy*, 2024, **5**, 100176, DOI: 10.1016/j.nxener.2024.100176.
43 Z. Liu, *et al.*, Unveiling the relationship between the multilayer structure of metallic MoS2 and the cycling performance for lithium ion batteries, *Nanoscale*, 2022, **14**(24), 8621–8627, DOI: 10.1039/D2NR00967F.
44 H. Chen, *et al.*, Si-based anode with hierarchical protective function and hollow ring-like carbon matrix for high performance lithium ion batteries, *Appl. Surf. Sci.*, 2019, **470**, 496–506, DOI: 10.1016/j.apsusc.2018.11.065.
45 N. Mahmood, C. Zhang, H. Yin and Y. Hou, Graphene-based nanocomposites for energy storage and conversion

in lithium batteries, supercapacitors and fuel cells, *J. Mater. Chem. A*, 2014, **2**(1), 15–32.
46 T. Irshad, *et al.*, Metal–organic frameworks for energy storage applications: recent advances, *J. Chin. Chem. Soc.*, 2023, **70**(9), 1692–1714, DOI: 10.1002/jccs.202300115.
47 Z. A. Sandhu, *et al.*, Metal–organic frameworks for next-generation energy storage devices; a systematic review, *Mater. Adv.*, 2024, **5**(1), 30–50, DOI: 10.1039/D3MA00822C.
48 W. Qi, J. G. Shapter, Q. Wu, T. Yin, G. Gao and D. Cui, Nanostructured anode materials for lithium-ion batteries: principle, recent progress and future perspectives, *J. Mater. Chem. A*, 2017, **5**(37), 19521–19540, DOI: 10.1039/C7TA05283A.
49 M. I. Khan, G. Nadeem, A. Majid and M. Shakil, A DFT study of bismuthene as anode material for alkali-metal (Li/Na/K)-ion batteries, *Mater. Sci. Eng., B*, 2021, **266**, 115061, DOI: 10.1016/j.mseb.2021.115061.
50 Y. R. Lim, *et al.*, Arsenic for high-capacity lithium-and sodium-ion batteries, *Nanoscale*, 2018, **10**(15), 7047–7057.
51 Y. Hou, S. Ma, Y. Xu, S. Zhang, X. Hao and B. Xu, Electrochemical Performance of Graphene Oxide/Black Arsenic Phosphorus/Carbon Nanotubes as Anode Material for LIBs, *Materials*, 2022, **15**(13), 4576, available, https://www.mdpi.com/1996-1944/15/13/4576.
52 N. Khossossi, *et al.*, High-Specific-Capacity and High-Performing Post-Lithium-Ion Battery Anode over 2D Black Arsenic Phosphorus, *ACS Appl. Energy Mater.*, 2021, **4**(8), 7900–7910, DOI: 10.1021/acsaem.1c01247.
53 K. Fan, J. Tang and Q. Sun, Monolayer Mo2C as anodes for magnesium-ion batteries, *J. Mol. Model.*, 2020, **26**(4), 86, DOI: 10.1007/s00894-020-4347-2.
54 R. Zainul, *et al.*, Evaluation of orthorhombic dialuminium dinitride as electrode material for magnesium ion batteries, *Inorg. Chem. Commun.*, 2025, **175**, 114115, DOI: 10.1016/j.inoche.2025.114115.
55 J. Liu, *et al.*, Ge/C nanowires as high-capacity and long-life anode materials for Li-ion batteries, *ACS Nano*, 2014, **8**(7), 7051–7059.
56 H. Yang, L. Liu, J. Ma, J. Zhang and Q. Zhang, Hydrothermal Synthesis of Hierarchical Cage-like Co9S8 Microspheres Composed of Nanosheets as High-Capacity Anode Materials, *Energies*, 2024, **17**(22), 5553.
57 Y. Shao, *et al.*, Highly Reversible Mg Insertion in Nanostructured Bi for Mg Ion Batteries, *Nano Lett.*, 2014, **14**(1), 255–260, DOI: 10.1021/nl403874y.
58 Y.-H. Tan, *et al.*, High Voltage Magnesium-ion Battery Enabled by Nanocluster Mg3Bi2 Alloy Anode in Noncorrosive Electrolyte, *ACS Nano*, 2018, **12**(6), 5856–5865, DOI: 10.1021/acsnano.8b01847.
59 J. Niu, *et al.*, Composition- and size-modulated porous bismuth–tin biphase alloys as anodes for advanced magnesium ion batteries, *Nanoscale*, 2019, **11**(32), 15279–15288, DOI: 10.1039/C9NR05399A.
60 M. F. Hughes, B. D. Beck, Y. Chen, A. S. Lewis and D. J. Thomas, Arsenic Exposure and Toxicology: A Historical Perspective, *Toxicol. Sci.*, 2011, **123**(2), 305–332, DOI: 10.1093/toxsci/kfr184.
61 A. Babayigit, A. Ethirajan, M. Muller and B. Conings, Toxicity of organometal halide perovskite solar cells, *Nat. Mater.*, 2016, **15**(3), 247–251, DOI: 10.1038/nmat4572.
62 S. Wu, *et al.*, Mesopore Controls the Responses of Blood Clot-Immune Complex via Modulating Fibrin Network, *Adv. Sci.*, 2022, **9**(3), 2103608, DOI: 10.1002/advs.202103608.
63 A. Van der Ven, Z. Deng, S. Banerjee and S. P. Ong, Rechargeable Alkali-Ion Battery Materials: Theory and Computation, *Chem. Rev.*, 2020, **120**(14), 6977–7019, DOI: 10.1021/acs.chemrev.9b00601.
64 G. C. A. da Hora, R. L. Longo and J. B. P. da Silva, Calculations of structures and reaction energy profiles of As2O3 and As4O6 species by quantum chemical methods, *Int. J. Quantum Chem.*, 2012, **112**(20), 3320–3324.
65 M. Elstner, *et al.*, Self-consistent-charge density-functional tight-binding method for simulations of complex materials properties, *Phys. Rev. B:Condens. Matter Mater. Phys.*, 1998, **58**(11), 7260.
66 H. Jónsson, G. Mills and K. W. Jacobsen, Nudged elastic band method for finding minimum energy paths of transitions, in *Classical and Quantum Dynamics in Condensed Phase Simulations*, World Scientific, 1998, pp. 385–404.
67 H. Lee, *et al.*, Understanding the effects of diffusion coefficient and exchange current density on the electrochemical model of lithium-ion batteries, *Curr. Opin. Electrochem.*, 2022, **34**, 100986.
68 D. Porezag, T. Frauenheim, T. Köhler, G. Seifert and R. Kaschner, Construction of tight-binding-like potentials on the basis of density-functional theory: application to carbon, *Phys. Rev. B:Condens. Matter Mater. Phys.*, 1995, **51**(19), 12947.
69 R. Gao, Z. Hu, J. Mao, S. Chen, C. Yam and G. Chen, Self-consistent-charge density-functional tight-binding parameters for modeling an all-solid-state lithium battery, *J. Chem. Theory Comput.*, 2023, **19**(5), 1381–1387.
70 J. Park and S. A. Fatima, A DFT study of TiC3 as anode material for Li-ion batteries, *Appl. Surf. Sci.*, 2023, **638**, 158024.
71 A. Kubaib and P. M. Imran, Application of lithium and a few relevant electrolytes evaluated as secondary batteries studied using molecular descriptors, band structure and DOS, *J. Mater. Sci.*, 2023, **58**(9), 4005–4019.
72 J. P. Perdew, K. Burke and M. Ernzerhof, Generalized Gradient Approximation Made Simple, *Phys. Rev. Lett.*, 1996, **77**(18), 3865–3868, DOI: 10.1103/PhysRevLett.77.3865.
73 A. Majid, N. Z. Raza, S. Ahmad and M. Alkhedher, Electrochemical performance of P4Se3 as high-capacity anode materials for monovalent and multivalent ion batteries, *Mater. Chem. Phys.*, 2024, **322**, 129515.
74 M. G. Kim and J. Cho, Reversible and High-Capacity Nanostructured Electrode Materials for Li-Ion Batteries, *Adv. Funct. Mater.*, 2009, **19**(10), 1497–1514, DOI: 10.1002/adfm.200801095.
75 H. Pan, A. Sheng, Z. Wang and X. Han, Analysis of MTBF evaluation methods for small sample sizes, in *2016 11th*

International Conference on Reliability, Maintainability and Safety (ICRMS), 2016, pp. 1–7, DOI: 10.1109/ICRMS.2016.8050042.

76 A. Majid, U. Najam, S. Ahmad and M. Alkhedher, On the prospects of using B4C3 as a potential electrode material for lithium-ion batteries, *Mater. Sci. Semicond. Process.*, 2024, **176**, 108320.

77 B. R. Karimadom, D. Meyerstein and H. Kornweitz, Calculating the adsorption energy of a charged adsorbent in a periodic metallic system – the case of BH4− hydrolysis on the Ag(111) surface, *Phys. Chem. Chem. Phys.*, 2021, **23**(45), 25667–25678, DOI: 10.1039/D1CP03895H.

78 N. Ehteshami, A. Eguia-Barrio, I. de Meatza, W. Porcher and E. Paillard, Adiponitrile-based electrolytes for high voltage, graphite-based Li-ion battery, *J. Power Sources*, 2018, **397**, 52–58, DOI: 10.1016/j.jpowsour.2018.07.004.

79 X. Li, *et al.*, Theoretical investigation of Mo2C and Mo2CO2 as anodes for sodium/magnesium-ion batteries, *J. Energy Storage*, 2024, **87**, 111500, DOI: 10.1016/j.est.2024.111500.

80 S. Alvin, C. Chandra and J. Kim, Controlling intercalation sites of hard carbon for enhancing Na and K storage performance, *Chem. Eng. J.*, 2021, **411**, 128490.

81 Y. Wu, S. Wang, Y. Xie, X. Ye and S. Sun, Highly stable TiOF monolayer as anode material for the applications of Li/Na-ion batteries, *Appl. Surf. Sci.*, 2022, **574**, 151296, DOI: 10.1016/j.apsusc.2021.151296.

82 H. Cho, C. Yoo and B. Shong, Influence of Ge precursors toward atomic layer deposition of germanium tellurides: a DFT study, *Vacuum*, 2025, **235**, 114142, DOI: 10.1016/j.vacuum.2025.114142.

83 M. M. Islam and T. Bredow, Density Functional Theory Study for the Stability and Ionic Conductivity of Li2O Surfaces, *J. Phys. Chem. C*, 2009, **113**(2), 672–676, DOI: 10.1021/jp807048p.

84 S. S. Naghavi, V. I. Hegde and C. Wolverton, Diffusion coefficients of transition metals in fcc cobalt, *Acta Mater.*, 2017, **132**, 467–478.

85 S. Parvarinezhad and M. Salehi, Synthesis, characterization, crystal structures, Hirshfeld surface analysis and DFT computational studies of new Schiff Bases derived from phenylhydrazine, *J. Mol. Struct.*, 2020, **1222**, 128780.

86 N. Z. Raza, A. Majid, A. Jabeen, S. Haider and K. Alam, First principles study on interactions in inorganic molecular crystals at zero dimensions, *J. Mol. Struct.*, 2024, **1317**, 139102.

87 X. Wu, H. Zhang, J. Yanghe and S. Liu, VN Quantum Dots Anchored onto Carbon Nanofibers as a Superior Anode for Sodium Ion Storage, *Materials*, 2024, **17**(23), 6004, https://www.mdpi.com/1996-1944/17/23/6004.

88 H. V. Aposhian, R. A. Zakharyan, M. D. Avram, M. J. Kopplin and M. L. Wollenberg, Oxidation and detoxification of trivalent arsenic species, *Toxicol. Appl. Pharmacol.*, 2003, **193**(1), 1–8.

89 D. W. Smith, The antibonding effect, *J. Chem. Educ.*, 2000, **77**(6), 780.

90 H. Hwang, H. Kim and J. Cho, MoS2 Nanoplates Consisting of Disordered Graphene-like Layers for High Rate Lithium Battery Anode Materials, *Nano Lett.*, 2011, **11**(11), 4826–4830, DOI: 10.1021/nl202675f.

91 J. E. Huheey, The electronegativity of groups, *J. Phys. Chem.*, 1965, **69**(10), 3284–3291.

92 J. Zhao, Q. Du, S. Zhou and V. Kumar, Endohedrally doped cage clusters, *Chem. Rev.*, 2020, **120**(17), 9021–9163.

93 S. Zhao, *et al.*, Adsorption mechanism of As2O3 on metal oxides (CaO, γ-Al2O3, α-Fe2O3): a density functional theory study, *Appl. Surf. Sci.*, 2023, **641**, 158472.

94 W. J. Schipper, Process for the Manufacture of P4O6 with Improved Yield, *US Pat.*, 8551437, 2013.

95 P. Atkins, *Shriver and Atkins' Inorganic Chemistry*, Oxford University Press, USA, 2010.

96 Y. Tan, L. Chen, H. Chen, Q. Hou and X. Chen, Synthesis of a symmetric bundle-shaped Sb2O3 and its application for anode materials in lithium ion batteries, *Mater. Lett.*, 2018, **212**, 103–106, DOI: 10.1016/j.matlet.2017.10.080.

97 K. Liu, Y. Liu, D. Lin, A. Pei and Y. Cui, Materials for lithium-ion battery safety, *Sci. Adv.*, 2018, **4**(6), eaas9820, DOI: 10.1126/sciadv.aas9820.

98 T. Hansson, C. Oostenbrink and W. van Gunsteren, Molecular dynamics simulations, *Curr. Opin. Struct. Biol.*, 2002, **12**(2), 190–196.

99 A. Majid, N. Z. Raza, S. Ahmad and M. Alkhedher, Electrochemical Performance of P4Se3 as High-Capacity Anode Materials for Monovalent and Multivalent Ion Batteries, *Mater. Chem. Phys.*, 2024, **322**, 129515.

100 I. Ahmed and A. Majid, Harnessing chromium oxychloride for next-generation monovalent and multivalent ion batteries: first principles investigations, *Mater. Sci. Semicond. Process.*, 2025, **192**, 109413, DOI: 10.1016/j.mssp.2025.109413.

101 R. E. Hummel, *Electronic Properties of Materials*, Springer Science & Business Media, 2011.

102 P. Borlido, T. Aull, A. W. Huran, F. Tran, M. A. L. Marques and S. Botti, Large-Scale Benchmark of Exchange-Correlation Functionals for the Determination of Electronic Band Gaps of Solids, *J. Chem. Theory Comput.*, 2019, **15**(9), 5069–5079, DOI: 10.1021/acs.jctc.9b00322.

103 X. Zhao, *et al.*, Study of electrochemical properties, mechanical properties, and lithium ion diffusion of Ni and N co- doped LiFePO4 based on first principles, *Comput. Theor. Chem.*, 2025, **1248**, 115236, DOI: 10.1016/j.comptc.2025.115236.

104 Y. Liu, S. P. Jiang and Z. Shao, Intercalation pseudocapacitance in electrochemical energy storage: recent advances in fundamental understanding and materials development, *Mater. Today Adv.*, 2020, **7**, 100072.

105 L. Fan, H. L. Zhuang, W. Zhang, Y. Fu, Z. Liao and Y. Lu, Stable lithium electrodeposition at ultra-high current densities enabled by 3D PMF/Li composite anode, *Adv. Energy Mater.*, 2018, **8**(15), 1703360.

106 L. Jin, J. Zheng and J. P. Zheng, Theoretically quantifying the effect of pre-lithiation on energy density of Li-ion batteries, *J. Electrochem. Soc.*, 2021, **168**(1), 010532.

107 M. Wang, F. Zhang, C. S. Lee and Y. Tang, Low-cost metallic anode materials for high performance rechargeable batteries, *Adv. Energy Mater.*, 2017, **7**(23), 1700536.
108 A. Ullah, A. Majid and N. Rani, A review on first principles based studies for improvement of cathode material of lithium ion batteries, *J. Energy Chem.*, 2018, **27**(1), 219–237.
109 N. Nitta, F. Wu, J. T. Lee and G. Yushin, Li-ion battery materials: present and future, *Mater. Today*, 2015, **18**(5), 252–264, DOI: **10.1016/j.mattod.2014.10.040**.
110 N. A. Kaskhedikar, G. Cui, J. Maier, V. Fedorov, V. Makotchenko and A. Simon, *Superfine expanded graphite with large capacity for lithium storage*, 2011, pp. 523–529.
111 G. Henkelman, B. P. Uberuaga and H. Jónsson, A climbing image nudged elastic band method for finding saddle points and minimum energy paths, *J. Chem. Phys.*, 2000, **113**(22), 9901–9904.
112 X. Zhang, *et al.*, Monolayer GaS with high ion mobility and capacity as a promising anode battery material, *J. Mater. Chem. A*, 2019, **7**(23), 14042–14050.
113 W. Qin, W.-C. Lu, X.-Y. Xue, K.-M. Ho and C.-Z. Wang, Lithium Diffusion in Silicon Encapsulated with Graphene, *Nanomaterials*, 2021, **11**(12), 3397.
114 Z. Yang, *et al.*, Recent progress and prospect of Li-Se batteries: a comprehensive review, *Energy Materials*, 2023, **3**(3), 300027.
115 D. Li, Y. Yuan, J. Liu, M. Fichtner and F.-S. Pan, A review on current anode materials for rechargeable Mg batteries, *J. Magnesium Alloys*, 2020, **8**, 963–979, DOI: **10.1016/j.jma.2020.09.017**.
116 U. Kasavajjula, C. Wang and A. J. Appleby, Nano- and bulk-silicon-based insertion anodes for lithium-ion secondary cells, *J. Power Sources*, 2007, **163**(2), 1003–1039, DOI: **10.1016/j.jpowsour.2006.09.084**.
117 S. Plimpton, Fast Parallel Algorithms for Short-Range Molecular Dynamics, *J. Comput. Phys.*, 1995, **117**(1), 1–19, DOI: **10.1006/jcph.1995.1039**.
118 D. Frenkel and B. Smit, *Understanding Molecular Simulation: From Algorithms to Applications*, Elsevier, 2023.
119 Z. P. Bažant, Structural stability, *Int. J. Solids Struct.*, 2000, **37**(1–2), 55–67.
120 S. Scally, W. Davison and H. Zhang, Diffusion coefficients of metals and metal complexes in hydrogels used in diffusive gradients in thin films, *Anal. Chim. Acta*, 2006, **558**(1), 222–229, DOI: **10.1016/j.aca.2005.11.020**.
121 D.-T. Nguyen and S.-W. Song, Magnesium stannide as a high-capacity anode for magnesium-ion batteries, *J. Power Sources*, 2017, **368**, 11–17, DOI: **10.1016/j.jpowsour.2017.09.054**.
122 Y. Cheng, *et al.*, Interface promoted reversible Mg insertion in nanostructured Tin–Antimony Alloys, *Adv. Mater.*, 2015, **27**(42), 6598–6605.
123 H. Yang and N. Wu, Ionic conductivity and ion transport mechanisms of solid-state lithium-ion battery electrolytes: a review, *Energy Sci. Eng.*, 2022, **10**(5), 1643–1671.
124 J. Niu, *et al.*, Composition-and size-modulated porous bismuth–tin biphase alloys as anodes for advanced magnesium ion batteries, *Nanoscale*, 2019, **11**(32), 15279–15288.
125 K. V. Kravchyk, *et al.*, Colloidal Bismuth Nanocrystals as a Model Anode Material for Rechargeable Mg-Ion Batteries: Atomistic and Mesoscale Insights, *ACS Nano*, 2018, **12**(8), 8297–8307, DOI: **10.1021/acsnano.8b03572**.
126 J. Nam, H. Lee and O. B. Chae, Overcoming Challenges in Silicon Anodes: The Role of Electrolyte Additives and Solid-State Electrolytes, *Micromachines*, 2025, **16**(7), 800, available, **https://www.mdpi.com/2072-666X/16/7/800**.
127 M. Liang, Y. Fu, R. Gao, Q. Wang and J. Nie, Ellipsoidal Abstract and Illustrative Representations of Molecular Surfaces, *Int. J. Mol. Sci.*, 2019, **20**(20), 5158, DOI: **10.3390/ijms20205158**.
128 J. B. Goodenough and Y. Kim, Challenges for Rechargeable Li Batteries, *Chem. Mater.*, 2010, **22**(3), 587–603, DOI: **10.1021/cm901452z**.
129 K.-Y. Liu, J. D. Baek, C. S. Ng and P.-C. Su, Improving thermal stability of nanoporous platinum cathode at platinum/yttria-stabilized zirconia interface by oxygen plasma treatment, *J. Power Sources*, 2018, **396**, 73–79, DOI: **10.1016/j.jpowsour.2018.06.018**.
130 W. Falek, *et al.*, A structural comparative study of charge transfer compounds: synthesis, crystal structure, IR, Raman-spectroscopy, DFT computation and Hirshfeld surface analysis, *J. Mol. Struct.*, 2019, **1192**, 132–144.
131 G. T. Te Velde, F. M. Bickelhaupt, E. J. Baerends, C. F. Guerra, S. J. van Gisbergen, J. G. Snijders and T. Ziegler, *Amsterdam Density Functional (ADF)*, 2001, **https://www.scm.com**.